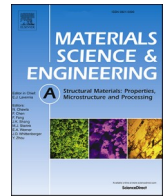




Contents lists available at ScienceDirect

## Materials Science &amp; Engineering A

journal homepage: <http://www.elsevier.com/locate/msea>

# Experimental validation and microstructure characterization of topology optimized, additively manufactured SS316L components

B. Rankouhi<sup>a</sup>, K.M. Bertsch<sup>b</sup>, G. Meric de Bellefon<sup>b,c</sup>, M. Thevamaran<sup>c</sup>, D.J. Thoma<sup>a,b,c</sup>, K. Suresh<sup>a,\*</sup>

<sup>a</sup> Department of Mechanical Engineering, University of Wisconsin-Madison, Madison, WI, 53706, USA

<sup>b</sup> Department of Materials Science and Engineering, University of Wisconsin-Madison, Madison, WI, 53706, USA

<sup>c</sup> Grainger Institute for Engineering, University of Wisconsin-Madison, Madison, WI, 53706, USA

## ARTICLE INFO

## Keywords:

Topology optimization  
 Selective laser melting  
 Directed energy deposition  
 Mechanical characterization  
 Microstructure analysis  
 SS316L

## ABSTRACT

The integration of topology optimization (TO) and additive manufacturing (AM) has the potential to revolutionize modern design and manufacturing. However, few instances of manufactured optimized designs are documented, and even fewer examples of experimentally-tested designs are available. The lack of validation combined with the influence of AM process on material properties leaves a gap in our understanding of process-microstructure-property relationships that is essential for developing holistic design optimization frameworks. In this work, a functional design was topologically optimized and fabricated using both directed energy deposition (DED) and selective laser melting (SLM) methods. This is the first direct comparison of these AM methods in the context of TO. Mechanical properties of SS316L and the optimized components in as-fabricated and heat-treated conditions were investigated under uniaxial displacement-controlled tensile loading and compared to finite element modeling (FEM) predictions. Optimized samples provided regions of both compressive and tensile loading in the test specimen. Experimental results showed the FEM predictions to be conservative. Microstructural analysis revealed that this difference is due to refined microstructures formed during the additive manufacturing process that strengthen the material in regions with high stress levels. Moreover, SLM samples showed higher yield strength compared to DED samples due to a more refined grain size and denser dislocation structures. TO results are sensitive to the AM method, post-processing conditions, and differences in mechanical properties. Thus, a TO for AM framework can be best optimized with the incorporation of microstructure features to account for localized microstructural variations in fabricated components.

## 1. Introduction

### 1.1. Motivation

Additive manufacturing (AM) can allow fabrication of designs that were previously impossible using conventional methods. AM technology has evolved as the manufacturing sector's adoption rate has grown by 80% since 2016 [1]. Benson et al. [2] investigated the improvement rate of AM technology based on the number of approved patents and determined that it is on an exponential growth rate, particularly with respect to manufacturing time and cost [3]. The increasing popularity of AM has also revitalized topology optimization (TO) [4]. TO is a mathematical technique in which material from a model of a structural component is selectively altered or removed to reduce weight while

maintaining mechanical integrity or satisfying a geometrical constraint. Most geometrically complex designs generated by TO can only be manufactured through AM methods. As a result, TO is receiving growing attention among design engineers who are seeking to leverage the advantages of AM. Some of the recent attempts in design for AM (DfAM) include overhang-free designs which reduce or eliminate the need for support structures [5,6], diversified TO methods for porous metal structures [7], design with AM-induced anisotropy considerations [8,9], and microstructure control with TO Ref. [4]. However, resulting models are seldom manufactured and tested; see Refs. [10–12] for exceptions. This lack of experimental validation leaves a gap in our understanding of AM process-structure-properties-performance (PSPP) relationship and how it influences design optimization paradigms. More importantly, this knowledge gap prevents us from achieving a holistic design paradigm

\* Corresponding author.

E-mail address: [ksuresh@wisc.edu](mailto:ksuresh@wisc.edu) (K. Suresh).

<https://doi.org/10.1016/j.msea.2020.139050>

Received 27 August 2019; Received in revised form 10 January 2020; Accepted 3 February 2020

Available online 5 February 2020

0921-5093/© 2020 Elsevier B.V. All rights reserved.

that couples design optimization with materials and process capabilities of AM [13].

This work aims to bridge the gap between design optimization and AM communities by realizing the light-weighting capabilities of TO through experimental validation of optimal designs. For the first time, this work directly compares the mechanical performance of topology optimized functional parts, manufactured via selective laser melting (SLM) and directed energy deposition (DED). We discuss the microstructure differences and similarities of both AM methods and their contribution to mechanical performance of TO parts. Furthermore, we provide insight into how novel AM microstructures influence the mechanical properties that are essential in TO and how this understanding should inform the decision-making in DfAM. Finally, a quantitative connection between AM method, microstructure, and mechanical properties is established to explain the discrepancies between the finite element modeling (FEM) and the experimental results.

## 1.2. TO for AM

SLM and DED each provide advantages over conventional processes. SLM is used for the freedom in design offered due to its high precision and capability to create support structures for overhanging surfaces [14]. DED offers limited geometrical design freedom, since it cannot create overhanging features and the minimum feature size is up to ten times larger than that in SLM [14]. However, powder deposition in DED allows for instantaneous or gradual modification of the deposited composition, resulting in the ability to manufacture compositionally graded structures or high-throughput testing of new alloys in different designs [15–18]. Functional grading has the potential to allow for an additional layer of complexity in design optimization. For example, Mirzendehtdel and Suresh [19] showed that multi-material TO can yield stiffer designs for a given volume fraction of material compared to single-material TO. Therefore, the ability to manufacture load-bearing, functional parts with DED allows us to take advantage of the unique mechanical, metallurgical and functionally graded properties of DED.

Variability in AM machines and the dependence of mechanical properties on microstructure mean that mechanical performance of a part can largely vary depending on the type of AM unit as well as what set of parameters or post-processing methods are used [20–24]. The mechanical response, particularly the yield strength and stiffness, has been shown to vary as a function of build orientation, heat-treatment method, and process parameters [25–32]. For example, the documented mechanical properties of AM SS316L, shown in Table 1, differ from those of conventionally manufactured SS316L and vary significantly between different AM methods. As a result, it is possible to compute different optimal topologies for the same design due to variations in the Young's modulus and yield strength.

**Table 1**

Comparison of SS316L tensile properties as reported by machine manufacturer with those given in the literature.

Properties	Values <sup>a</sup>			
	SLM		DED	
	Machine Manufacturer	Literature [22]	Machine Manufacturer	Literature [40,41]
Young's modulus (E) GPa	typ. 185	188 ± 29	-	193
Ultimate tensile strength (UTS) MPa	640 ± 50	592 ± 69	799	685 ± 66
Yield strength (Y) MPa	530 ± 60	453 ± 54	500	465 ± 78
Elongation (ε) %	40 ± 15	30 ± 6	50	35 ± 3

Annealed bar ASTM SS316L: UTS = 485 MPa, Y = 170 MPa, ε = 40% [42].

<sup>a</sup> Values are obtained from as-built tensile samples, pulled perpendicular to build direction (Fig. 1).

Examples of optimal designs are shown in Table 2. These designs are obtained using mechanical properties reported in Table 1. For the design obtained from ASTM properties, the target volume fraction is not achieved due to significantly lower yield strength. For designs obtained from SLM and DED properties, the final topology depends on which mechanical properties are selected by the user. These designs signify the need for mechanical properties characterization prior to TO. Moreover, the variance in mechanical properties and its influence on TO indicates that design optimization solutions should encompass these variations to ensure accuracy and robustness. Until such design solutions are available, developing widely applicable predictions of mechanical performance for optimized designs fabricated via AM will remain a challenge [13].

## 1.3. AM microstructure

The rapid, directional solidification and complex thermal cycling in both SLM and DED processes modify microstructural development compared to conventionally-fabricated materials [32]. In SLM parts, the synthesis leads to a dense, cellular dislocation microstructure and the formation of small precipitates as well as typically high yield strength and ductility [33]. Less is known about the microstructure in DED parts, although they have also been shown to exhibit a high yield strength [32]. Although the influence of characteristics such as grain size, texture, and dislocation structure development on mechanical response have been phenomenologically investigated extensively in conventional materials, the physical relationships between the AM microstructures and the improved mechanical response are less defined. Several efforts have been made to predict the resulting mechanical properties of AM material by microstructure characterization [29,33–39]. Currently, these approaches are time consuming, cost prohibitive and impractical in an industrial setting. However, they highlight an untapped potential of AM to locally control material properties at voxel level whereby AM process, microstructure, and mechanical properties can be incorporated in design optimization [13]. Such optimization schemes can produce designs that meet requirements with margins, but first, the gap in our understanding of PSPP relationship must be filled.

## 2. Materials and methods




### 2.1. Mechanical properties characterization

SS316L is a commonly used material in AM and thus it was chosen for this study. The stainless-steel alloy does not experience any solid-state phase transformations during deformation, and the alloy is nominally single-phase after manufacture. To characterize the mechanical properties of the AM materials, tensile test specimens (Fig. 1) were mechanically ground on both sides with sandpaper to 600 grit, then additionally on one side with diamond, alumina, and finally 0.05 μm colloidal silica grits to minimize the effects of surface roughness and possible mechanical damage from electrical discharge machining (EDM) used to remove the samples from the build plate. Room temperature tensile tests were performed using an MTS® Sintech load frame with a 50 kN load cell and 2.20 mV/V sensitivity. Tests were carried out at constant cross-head separation rate of 1 mm/min (strain rate of 0.04 s<sup>-1</sup>) and data were collected at 10 Hz. Strain measurements were conducted by digital image correlation (DIC) system provided by Correlated Solutions®. Zero-normalized squared difference algorithm was used to calculate the displacement of speckles on each sample. Collected data were then translated to longitudinal principal strains. Results were used to calculate the mechanical properties of SS316L in the elastic regime, including the Young's modulus and yield strength (calculated based on the 0.2% offset method).

In mechanical testing of topology-optimized parts, the same procedure was followed as for the tensile test specimens; however, to accurately capture part displacement and avoid adding the fixture strain

**Table 2**

Examples of possible optimal topologies obtained from select mechanical properties reported in Table 1. Volume fraction is defined as the volume of the original design divided by the volume of the final design.

	Mechanical Properties used in TO as reported by		
	ASTM	SLM	DED
Desired % vol. fraction	50	50	50
Topology			
% vol. fraction achieved	32	50	50

to the data set, an MTS extensometer with gauge length of 25 mm and travel range of (+12.5, -2.5) mm was used. Force-displacement data was collected for further analysis.

**2.2. Topology optimization**

Three criteria were considered for selecting the suitable case study. First, the part geometry should allow the use of a simple test fixture without the need for assembly. Using intricate testing fixtures alters the load distribution path throughout the part and can cause premature

failure in assembled joints [11]. Moreover, complex fixtures can hinder our ability to accurately measure force and displacement during testing. Second, the component should be a load-bearing part that represents real world scenarios where both compressive and tensile stresses are present. Third, the final topology should be manufacturable via both SLM and DED methods. The clevis part that meets the above-mentioned criteria was chosen for optimization. Fig. 2 shows the model’s critical dimensions and the selected boundary conditions (BCs).

The TO algorithm used in this work is Pareto, developed at UW-Madison [43], now commercially available ([www.sciartsoft.com](http://www.sciartsoft.com)). Pareto is a topological-sensitivity based method that can generate numerous Pareto-optimal topologies up to a desired volume fraction. Readers are referred to Refs. [43,44] for more details on the Pareto method. The TO problem is posed as below and solved with 100,000 hexahedral elements by taking advantage of symmetry.

$$\begin{aligned} & \text{Min } J \\ & \Omega \cap D \\ & \text{subject to} \\ & \text{stress, volume and manufacturing constraints} \end{aligned} \tag{1}$$

Where:

$$\begin{aligned} J & : \text{Compliance} \\ \Omega & : \text{Geometry/topology to be computed} \\ D & : \text{Design space} \end{aligned} \tag{2}$$

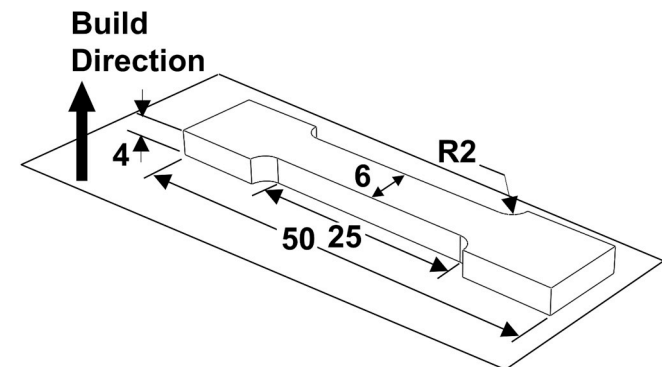


Fig. 1. Tensile test specimen geometry and build direction. Dimensions in (mm).

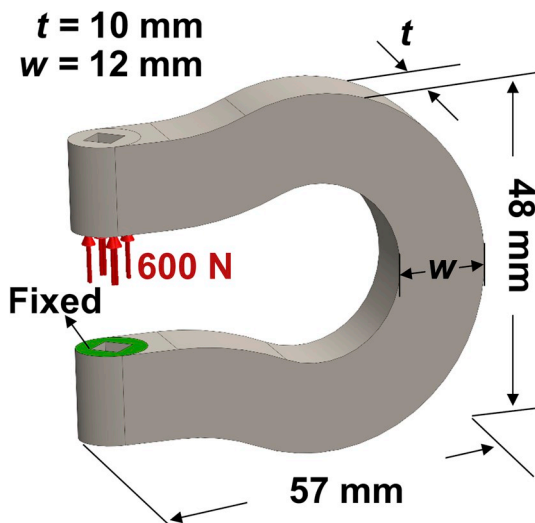


Fig. 2. Clevis model with critical dimensions and BCs.

In order to impose performance (stress) constraints, appropriate yield strengths for SLM and DED fabricated parts were determined using standard tensile testing described in section 2.1. In addition, an arbitrary volume fraction constraint of 50% was chosen for this case study. Here, the volume fraction is defined as the original volume of the design divided by the final volume of the design after TO.

The optimal topologies computed without explicit manufacturing constraints are not manufacturable via DED method due to the presence of hollow features. Although these designs can be fabricated via SLM, the hollow features prohibit the removal of required support structures, making them impractical for SLM as well (Fig. 3(a)). Thus, it was critical to impose manufacturing constraints on problem. A through-cut constraint was applied to ensure that the cross-section remained constant along the build direction, eliminating the need for support structures (Fig. 3(b)).

**2.3. Additive manufacturing**

**2.3.1. Selective laser melting**

An EOS® M290 system was used to manufacture six clevis samples using recommended process parameters in Table 3 [45]. It is known that SLM parts exhibit anisotropic behavior based on build direction [25], i. e. ultimate tensile strength is lower along the build direction. Therefore,

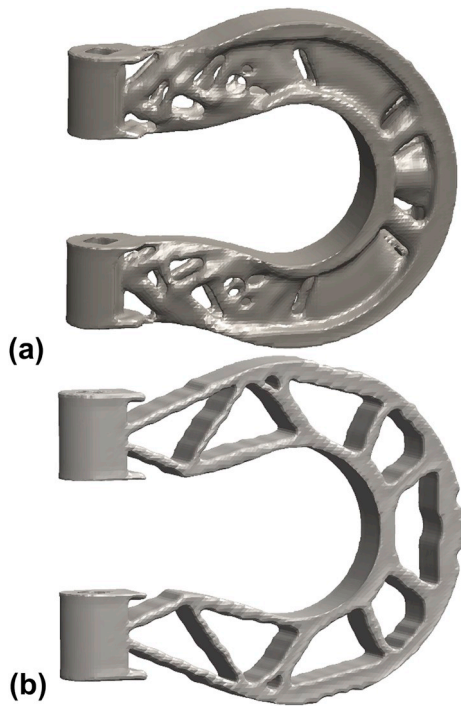


Fig. 3. An example of a topology optimized clevis part without imposing manufacturing constraints (a) and with through-cut constraint (b). The TO problem is posed as described in section 2.2.

Table 3  
EOS M290 main process parameters for SS316L.

Parameter	Values
Contour	2 layers
Laser power	
Infill	195 W
Contour	110 W
Laser speed	
Infill	1083 mm/s
Contour	800 mm/s
Hatch rotation angle	67°
Hatch distance	0.09 mm
Layer thickness	0.02 mm
Platform temperature	80 °C

samples were fabricated in the orientation perpendicular to the direction of applied force shown in Fig. 2 to mitigate the effects of anisotropy in tensile testing. Furthermore, six tensile specimens were cut using wire electrical discharge machining (EDM), from rectangular bars manufactured using the same build direction relative to the loading direction and process parameter set as clevises. Fig. 1 shows the dimensions of these specimens. In both cases, three samples were used as-built as a control while the other three were subjected to a heat treatment of 1000 °C for 1 h, followed by a water quench. Heat treatment process was in accordance with the procedure mentioned in Ref. [46]. Heat treatment is commonly used for AM parts to alleviate the effects of residual stresses on the mechanical properties [27,47].

The material used in manufacturing was SS316L powder, particle size less than 60 μm, provided by EOS®. Nominal chemical composition of the powder (as supplied) and as-built samples are presented in Table 4. Actual chemical compositions were measured with combustion infrared detection (C and Si), inert gas fusion (O and N), and direct current plasma emission spectroscopy (all others).

### 2.3.2. Directed energy deposition

An Optomec® laser engineered net shaping (LENS®) MR7 system

Table 4

Chemical composition of SS316L. Nominal values are reported by powder manufacturer while actual values are measured from as-built samples. All values are in wt%.

Element	SLM		Actual	DED		
	Nominal			Nominal	Actual	
	Min	Max				Min
Fe	Balance		Balance	Balance	Balance	
Cr	17.000	19.000	18.390	16.000	18.000	18.060
Ni	13.000	15.000	13.940	10.000	14.000	13.790
Mo	2.250	3.000	2.860	2.000	3.000	2.860
C	-	0.030	0.004	-	0.030	0.005
Mn	-	2.000	1.470	-	2.000	1.580
Cu	-	0.500	0.002	-	-	0.010
P	-	0.025	0.017	-	0.045	0.008
S	-	0.010	0.004	-	0.030	0.004
Si	-	0.750	0.300	-	1.000	0.320
N	-	0.100	0.065	-	-	0.072
O	-	-	0.043	-	-	0.037
H	-	-	0.00008	-	-	-
Co	-	-	0.0036	-	-	0.0054
Al	-	-	0.002	-	-	0.001

was used to manufacture clevis and tensile testing specimens using the same approach used for the SLM parts. The main process parameters used during manufacturing are presented in Table 5. Process-induced anisotropy has also been reported for parts manufactured via DED, although it is typically not as pronounced as with SLM [28]. The same build orientations used in the SLM approach were used for DED parts. Parts were cut off the build plates using wire EDM and rounded ends and holes were later machined. Tensile testing specimens were fabricated using the same process parameters in Table 5, and the same dimensions as depicted in Fig. 1, except for a thickness of 2.5 mm. The same sample size and heat-treatment process was repeated for the DED experiment. SS316L powder used for DED process was provided by Carpenter® with particle size range of 45 to 150 μm. The nominal composition of the DED powder and actual chemical composition of the samples are provided in Table 4.

### 2.4. Microstructural characterization

The influences of processing method and heat treatments on the microstructure were analyzed across multiple length scales to include microstructural characteristics known to influence the mechanical properties. Grain size and grain morphology were analyzed using scanning electron microscopy (SEM) in a Zeiss LEO-1 microscope operated at 3-20 kV accelerating voltage, as well as with electron backscatter diffraction (EBSD) in a FEI Helios G4 PFIB CXe with an Elstar™ SEM column equipped with an Hikari EBSD camera and accelerating voltage of 230 kV. EBSD maps were approximately 1-2 mm x 2-3 mm with step sizes of 1-3 μm. Some specimens were sectioned in the undeformed state and mechanically ground, then 3 mm disks were punched out. Disks were polished to electron transparency with a Stuers Tenupol twin-jet electropolisher in A2 electrolyte at -20 °C and 17 V for

Table 5  
Optomec® LENS MR7 main process parameters for SS316L.

Parameter	Values
Contour	2 layers
Contour offset	0.38 mm
Laser power	
Infill	275 W
Contour	275 W
Feed rate	508 mm/min
Hatch rotation angle	67°
Hatch distance	0.38 mm
Layer thickness	0.254 mm



approximately 15 min for TEM analysis. TEM samples were analyzed in a Tecnai TF-30 S/TEM operated at 300 kV for diffraction contrast imaging and diffraction analysis of dislocation structures and crystallography.

### 3. Results and analysis

#### 3.1. Tensile test results

The data in Table 6 presents the means and standard deviations of mechanical properties of SS316 tensile test specimens for SLM and DED. Stress-strain curves are presented in Fig. 4. Overall, the effect of heat treatment on both SLM and DED samples were similar with the yield strength as the most affected property. After heat treatment, the yield strength dropped by 49% and 50% for SLM and DED samples, respectively. Standard deviations indicated that DED demonstrated better consistency in mechanical properties in the elastic regime compared to SLM. However, the same cannot be said for elongation at failure, where DED showed larger deviations compared to SLM. It should be noted that further experiments are needed to confirm this initial observation and provide a scientific basis for this conclusion. Nonetheless, all samples indicated at least 40% elongation to failure in tension, and this ductility was more than adequate for the scope of this work.

#### 3.2. Clevis TO and mechanical test results

After mechanical properties characterization, TO was carried out using the reported Young's modulus and yield strength of heat-treated samples in Table 6. The final optimal designs for SLM and DED clevises obtained are shown in Table 7. It should be noted that the measured difference in Young's modulus and yield strength between SLM and DED resulted in a subtle difference in final designs. A comparison between Fig. 5(a) and Fig. 5(b) revealed that clevis design for SLM has 12 reinforcing struts distributed along its arch while clevis design for DED has 10. However, for a meaningful comparison, the design shown in Fig. 5(b) was chosen for fabrication using both AM methods.

Artifacts from the TO process were manifested as mesh irregularities, as shown in the inset in Fig. 5(b). These irregularities can cause stress concentration and premature failure during testing. As of today, fully automated feature-based geometry reconstruction for TO remains an unsolved problem [48–51]. Therefore, to alleviate the concerns regarding the mesh irregularities, the design shown in Fig. 5(b) was used as a reference to create the design shown in Fig. 5(c) using conventional CAD operations. It should be noted that this method of geometry reconstruction is limited to standard CAD operations and the resulting features may not fully capture the complexity of the original design. However, in this case study, the through-cut constraint simplified the design to a level that conventional CAD operations were able to closely capture the features of the original design. More importantly, as shown in Fig. 5(d), the maximum von Mises stress occurred on the outer surface of the clevis' arch, and this surface was unaffected during TO. As a result, this critical feature was perfectly preserved throughout the geometry reconstruction process. The final optimal designs were then manufactured using AM, as shown in Fig. 6.

Although the optimized design achieved the target of 50% volume

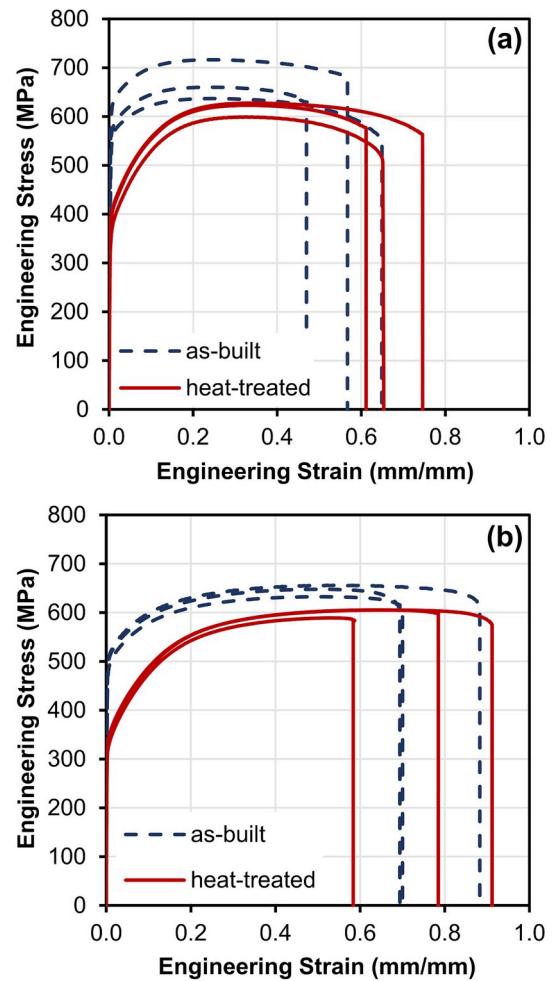


Fig. 4. Engineering stress-strain curves obtained from tensile test specimens. (a) SLM and (b) DED.

Table 7

Optimal topologies obtained from mechanical properties of heat-treated SS316L reported in Table 6.

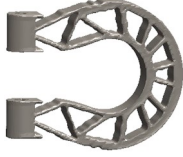

	Mechanical Properties used in TO	
	SLM	DED
Desired % vol. fraction	50	50
Topology		
% vol. fraction achieved	50	50

Table 6

Mechanical properties of SS316L, obtained from tensile test specimens.

		Young's modulus (E) GPa	Ultimate tensile strength (UTS) MPa	Yield strength (YS) MPa	Elongation at UTS (%)	Elongation at YS (%)
SLM	as-built	190 ± 45	671 ± 33	560 ± 25	24 ± 0.8	0.52 ± 0.07
	heat-treated	147 ± 32	616 ± 13	377 ± 19	33 ± 0.4	0.48 ± 0.06
DED	as-built	198 ± 16	645 ± 10	489 ± 8	52 ± 2	0.47 ± 0.02
	heat-treated	188 ± 12	600 ± 8	325 ± 4	60 ± 6	0.39 ± 0.02

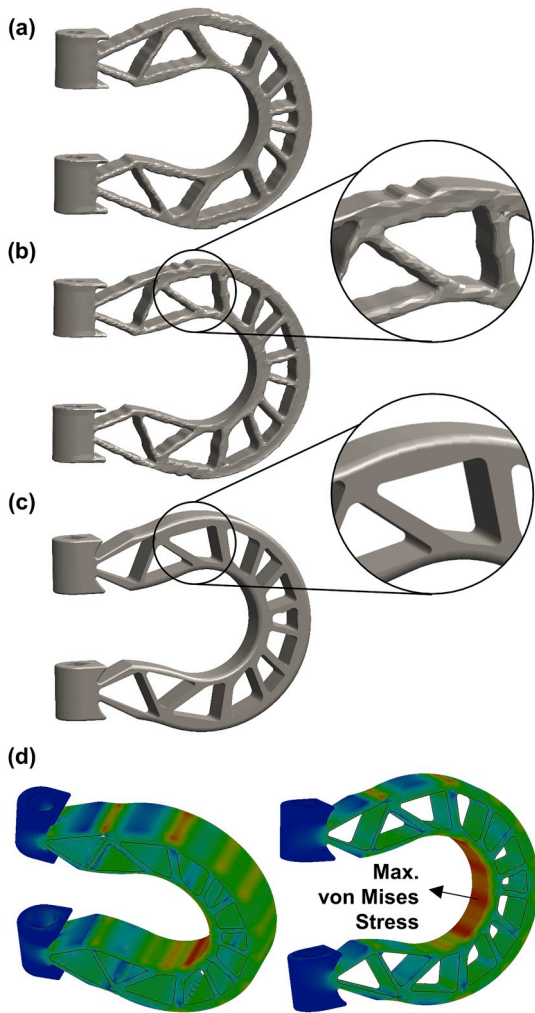


Fig. 5. TO designs based on the mechanical properties of (a) heat-treated DED, and (b) heat-treated SLM. (c) Design 'b' is reconstructed for AM using conventional CAD operations. (d) Different views of von Mises stress distribution. Area where maximum von Mises stress occurred is indicated by the arrow.

fraction, and the same model was used to manufacture the samples, the volume of manufactured clevises differed from the 50%. The average volume fraction of samples fabricated via SLM was measured at 45.6% while the average volume fraction of samples fabricated via DED was measured at 61.8%. The difference in the volume of the SLM samples is negligible and can be attributed to machining during support structure removal. The difference in the volume of the DED samples can be explained by considering the larger laser beam diameter of LENS system ( $\approx 600 \mu\text{m}$ ) compared to EOS system ( $\approx 80 \mu\text{m}$ ) which can result in oversized features in designs with intricate geometries.

The resulting force-displacement graphs from clevis tensile tests are shown in Fig. 7. Tests were terminated once the extensometer reached its maximum displacement. Heat-treated SLM samples yielded at

approximately 1500 N, compared to 1950 N for as-built samples. Similarly, heat-treated DED samples yielded at approximately 1710 N, compared to 2240 N for as-built samples. Results agree with the standard tensile test results wherein the heat-treatment process had a similar effect on the yield strength of both DED and SLM samples.

Finally, the data in Table 8 shows averaged results from the tensile tests against FEM using the properties presented in Table 6. Initially, results for DED samples showed larger deviation from FEM calculated values compared to SLM. The larger deviation can be attributed to the additional volume of the DED samples which increased the experimental yield load. To compensate for the increase in volume, the experimental yield loads of the DED samples were scaled. Since the thickness of the DED samples (denoted by  $t$  in Fig. 2) was kept the same after machining, the increase in volume was solely due to a uniform increase in the width (denoted by  $w$  in Fig. 2). According to basic bending stress calculations,

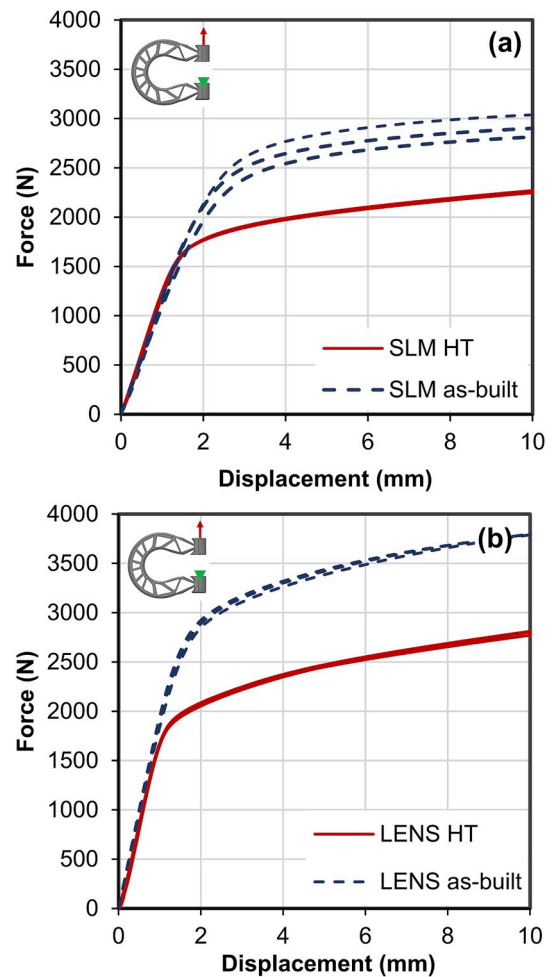


Fig. 7. Clevis tensile test results for (a) SLM and (b) DED fabricated samples, with and without heat treatment.

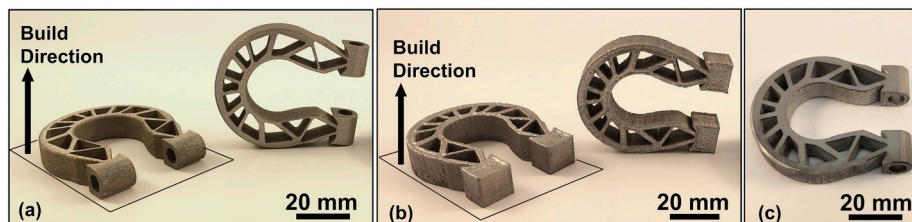


Fig. 6. Clevises manufactured via (a) SLM, and (b) DED. Round ends and holes for DED clevises were later machined to net shape (c).



**Table 8**  
Comparison of tensile test results with FEM for topology optimized clevises.

		FEM yield load (N)	Experimental yield load (N)	Scaled experimental yield load <sup>a</sup> (N)	Error <sup>b</sup> (%)
SLM	as-built	1825	1950	-	6.4
	heat-treated	1227	1500	-	18.2
DED	as-built	1590	2240	1680	5.7
	heat-treated	1058	1710	1282	21.2

<sup>a</sup> Experimental yield load for DED is scaled to reflect the increased volume of DED clevises during manufacturing.

<sup>b</sup> For DED, the error is based on the difference between the FEM and scaled yield loads.

11.8% increase in width results in 25% decrease in bending stress, and consequently, the yield load. After applying this adjustment, yield loads for both SLM and DED samples showed similar deviations from FEM predictions. Scaled yield loads for DED samples are presented in Table 8.

### 3.3. Microstructural characterization

The microstructures were found to be spatially heterogeneous in 3D and exhibited directionality dependence on the laser scan path and AM method. These dependencies are illustrated in the simplified schematic shown in Fig. 8 for reference. The following sections will frequently refer to this schematic and discuss the microstructural features depicted therein.

#### 3.3.1. Grain structure in SLM

The initial grain structures in the tensile test specimens indicated a strong dependence on laser scan direction, AM process, and thermal history, as shown in the EBSD maps in Fig. 9. These maps are colorized according to the crystallographic orientation aligned with the loading direction (vertical in Fig. 9) and the stereographic triangle color key (inset), with grain boundaries indicated in black. The as-built SLM structure consisted of grains that were columnar in the build direction, as indicated in Fig. 8, but exhibited a “mosaic” structure when viewed in the plane perpendicular to the build direction, as shown in Fig. 9(a). The mosaic structure, previously reported in steels manufactured using an EOS M270 SLM unit [52], consists of large grains (diameter greater than approximately 50  $\mu\text{m}$ ) aligned in rows along the laser scanning direction surrounded by small grains. Although large grains appeared equiaxed in the scanning plane shown in Fig. 9(a), many of the small grains were elongated along the laser scanning direction, yielding an average grain aspect ratio of 2.07 in the scanning plane. Grains were 20  $\mu\text{m}$  in diameter on average in the scanning plane. Grains were elongated in the build

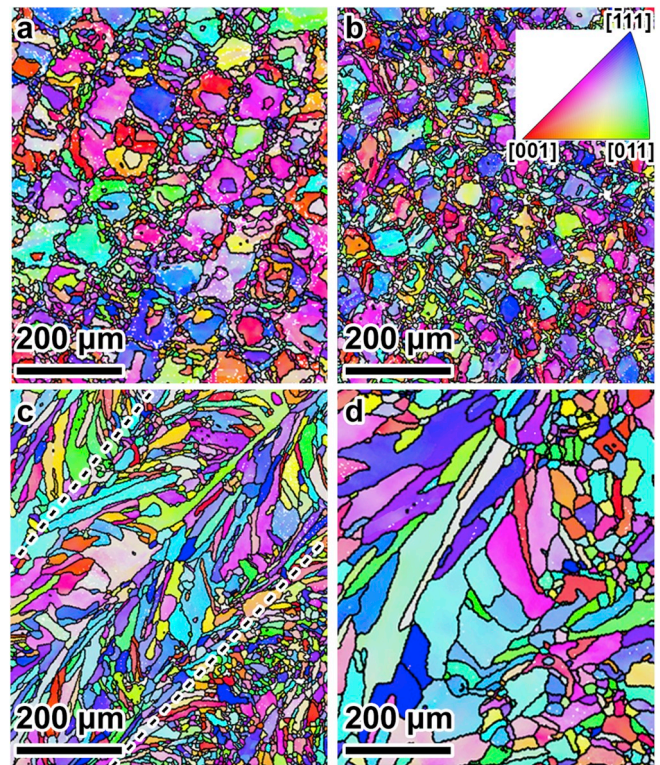


**Fig. 9.** EBSD orientation maps in the tensile loading direction of initial structures in (a) SLM as-built, (b) SLM heat-treated, (c) DED as-built, and (d) DED heat-treated tensile specimens, with grain boundaries indicated in black. Tensile axis vertical, build direction is out-of-plane. Dashed lines in (c) outline the edges of one laser scan path. Color online. (For interpretation of the references to color in this figure legend, the reader is referred to the Web version of this article.)

direction, typically reaching 100–400  $\mu\text{m}$  long, and extending across multiple layers. The grains appeared organized along the laser scanning direction, or 45° to the loading direction in the uniaxial tension specimens, as indicated parallel to the dashed lines in Fig. 9(a). There was no strong preferred orientation along the loading direction in the SLM as-built material. A  $\langle 011 \rangle$  texture developed in the build direction (out-of-plane in Fig. 9) in the SLM materials but this was not expected to strongly influence the tensile response, since there was no texture in the loading direction.

Heat treatment of the SLM material led to little change in grain size, with an apparent slight refinement from 20  $\mu\text{m}$  to approximately 16  $\mu\text{m}$  in diameter on average, Fig. 9(b). No significant change in the aspect

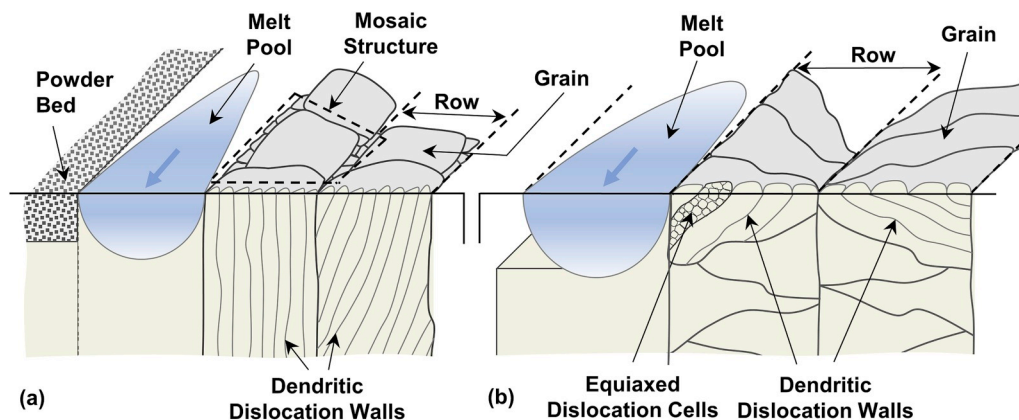


**Fig. 8.** Schematic illustrating laser scanning path, grain structure, and microstructural characteristics for (a) SLM and (b) DED fabricated parts.

ratio was observed in the scanning plane, although the mosaic structure became less apparent and the laser scanning path was no longer as evident in the final microstructure. The SLM microstructures have been shown to persist in annealing treatments up to 1200 °C for up to an hour [53–57], indicating high stability against heat treatment. The underlying mechanisms responsible for this enhanced stability in AM SS316L dislocation structures are still not fully understood, and are outside the scope of the current work. The slight refinement in grain size was likely a result of recovery processes and the inhibition of grain growth. Recovery and reorganization of deformation/dislocation microstructures, which are present in the as-built SLM material, can lead to an increased appearance of grain boundaries, as discussed in section 3.3.5. Despite the changes to the grain morphology, the original texture in the build direction was maintained after heat treatment in SLM material.

### 3.3.2. Grain structure in DED

The DED as-built structures consisted of elongated grains aligned approximately 20–30° to the laser scan direction, which was oriented approximately 45° to the loading axis, as indicated in Fig. 9(c) by dashed lines. Within each laser scanning pass, grains were elongated within ± 10° of the scan path, as indicated between the dashed lines in Fig. 9(c). The scan strategy of scanning 45° with respect to the sample loading axis, alternating 180° between passes and rotating 90° between layers, led to grains being elongated in various directions with respect to the loading axis dependent on the local laser scan direction. This directionality was also observed in the build direction, where grains were oriented either +45° or -45° with respect to the build direction depending on the layer, as shown schematically in Fig. 8(b). Grains exhibited an average aspect ratio of 3.09 in the laser scanning plane. Grains were elongated at various angles with respect to the build direction as well, in directions that changed depending on the layer, as indicated in Fig. 8. Although many grains were elongated, many regions between layers or between scan passes exhibited primarily equiaxed grains, as shown in the lower right corner of Fig. 9(c). The average grain

diameter for all grains, weighted by their respective areas, was approximately 80 μm. No significant texture was observed in the DED material. Heat treatment induced a significant increase in grain size, such that the average was approximately 140 μm, and a reduction in grain elongation, with an average aspect ratio of 2.14.

### 3.3.3. Comparison of response to heat treatment in SLM vs DED

The increase in grain size observed in DED material compared to the reduction observed in SLM material for the same heat treatment is considered to be a reflection of the microstructural differences. Differences between the initial dislocation structures likely influenced recovery and the formation of new grain boundaries, as discussed in section 3.3.5 and 3.3.6. However, differences in the microstructural evolution due to heat treatment are only relevant with respect to their influence on the mechanical response of heat-treated material; the mechanism responsible for any difference in the thermal stability of dislocation structures is outside the scope of this work. Together, these effects could have contributed to the difference in microstructural evolution between SLM and DED material subject to the same heat treatment.

### 3.3.4. Effects of scan strategy on grain structure

The influence of scan strategy on microstructure had an additional effect on the clevises due to the variations in relatively thinner and thicker sections of the design. EBSD maps of grain structures at the base of a strut in the clevis part are shown for SLM and DED as-built materials in Fig. 10(a) and (b), respectively. These maps are colorized according to the vertical loading direction using the same color key shown in Fig. 9, with grain boundaries traced in black. The region from which maps were taken on the clevis parts are shown in the inset; large black regions near the top left and lower right corners of Fig. 10(a) and (b) indicate empty space around the strut.

In the SLM material, grains were still organized along the laser-scanning path, as indicated parallel to the dashed lines in Fig. 10(a).

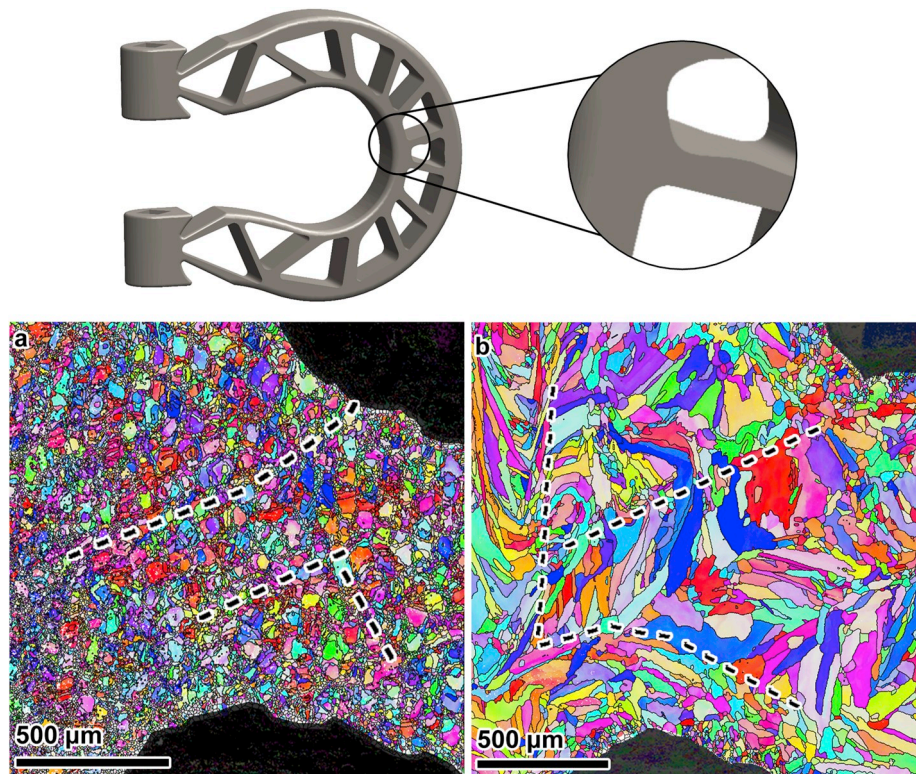


**Fig. 10.** EBSD orientation maps of initial structures in (a) SLM as-built and (b) DED as-built clevis parts. Colorized according to orientations in the loading direction (vertical). Color online. (For interpretation of the references to color in this figure legend, the reader is referred to the Web version of this article.)



However, the orientation of these rows changed in some regions, for example where the upper dashed line curves in Fig. 10(a). Another example is the orientation of rows in the thin strut compared to the bulk of the material, see dashed line in the lower section of Fig. 10(a). These changes in grain elongation direction were observed most frequently near the edges of the specimen, where different printing parameters and different scan strategies were used for contours; see Table 3. The dependence of the grain structure and elongation on laser scan path indicates an additional factor that may be considered when choosing scanning strategies for parts with complex geometries.

This influence of scan path was even more apparent in the DED parts, where grain alignment with the laser scanning path changed within approximately 400  $\mu\text{m}$  of edge of the part. Within 50–100  $\mu\text{m}$  of the edges, grains became smaller, as highlighted by the dashed lines in Fig. 10(b). The scanning strategy also influenced the grain elongation direction in different sections of the part's interior. For example, the grains at the leftmost side of Fig. 10(b) are finer than those in the middle of the strut, as indicated by dashed lines.

### 3.3.5. Dislocation microstructures in SLM

At the sub-grain level, microstructures influenced by AM processes were observed. In the SLM as-built material, a dislocation structure consisting of elongated, dendritic dislocation cells was observed, as shown in the bright-field STEM image in Fig. 11(a) and Fig. 8. Cell walls are indicated by dashed lines. The walls consisted of dense, tangled dislocations and tended to lie on {001}-type planes when viewed edge-on, as is typical for SLM 316L [33], with average spacing approximately 450 nm. The crystallographic directionality of the dislocation cells indicates that solidification was dendritic. Si, Mn, and Cr oxide precipitates were observed, typically ranging in size from 5–20 nm in diameter, examples of which are indicated by arrows in Fig. 11(a), as reported in Ref. [59]. In the as-built material, oxides were found to be primarily Si- and Mn-rich. The precipitates were observed both in cell interiors and within dislocation walls, although the density of precipitates was difficult to determine particularly inside walls due to the local density of dislocations. Precipitates frequently appeared to pin dislocations.

Heat treatment of SLM material qualitatively reduced the dislocation density and caused a reorganization of dislocation structures. Dislocation walls were observed, but with spacings typically ranging from 400–600 nm, slightly larger than that observed for the as-built material, as shown in Fig. 11(b). Higher-magnification imaging revealed that walls were qualitatively less dense than in the SLM as-built material, such that individual dislocations were more clearly defined and less tangled. Dislocation structures in the heat-treated specimens frequently corresponded to in-plane rotations of up to  $10^\circ$  between adjacent regions, which exceeds the threshold misorientation of  $3^\circ$  used to identify grain boundaries in EBSD mapping.

An example of these dislocation boundaries is shown in Fig. 11(b), where elongated boundaries can be seen aligned diagonally across the image. The diffraction pattern of this region, shown in the inset in Fig. 11(b), indicates that over approximately ten of these low-angle boundaries, in-plane rotations were measured up to approximately  $5.7^\circ$ . Many of the low-angle boundaries appeared to result from incomplete recovery and reorganization of the preexisting dislocation structures, such that they remained aligned and elongated. This is consistent with observations of the stability of the SLM microstructure against heat treatments below approximately  $1100^\circ\text{C}$  [53–57].

Dislocation structures within grains, in other words those that were unambiguously not part of a grain boundary, in SLM heat-treated material frequently consisted of aligned dislocations with fewer tangles than observed in SLM as-built dislocation cells. Example are indicated parallel to the dashed lines in Fig. 11(b). Oxide precipitates were larger in the heat-treated material, with sizes on the order of 40–60 nm, indicated by the arrows in Fig. 11(b). Precipitates in the heat-treated material were found via EDS analysis to be Cr- and Mn-rich oxides without

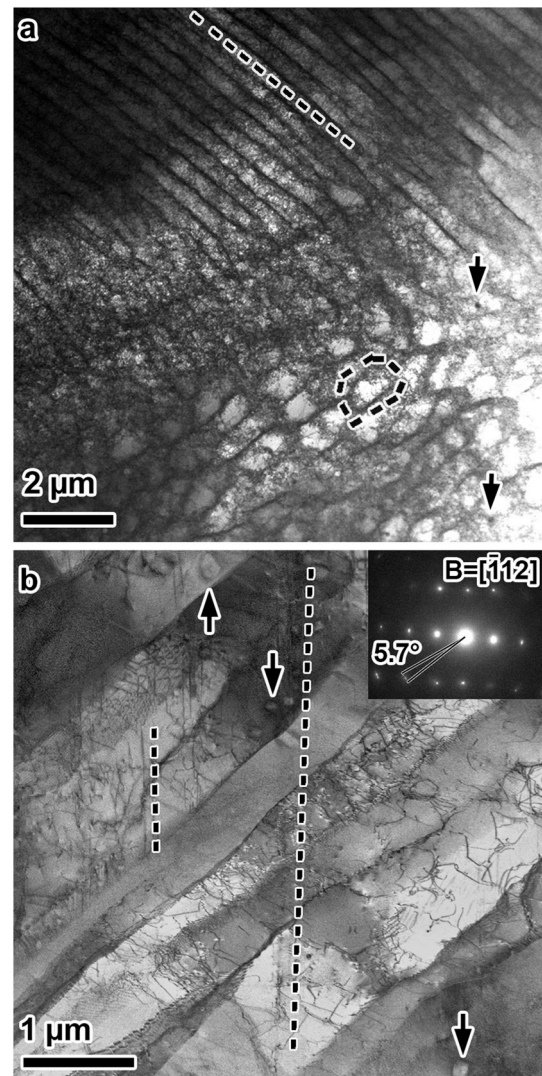


**Fig. 11.** Bright-field diffraction-contrast STEM images of dislocation structures in (a) SLM as-built material, with dendritic dislocation cells (dashed lines) and precipitates (arrows), and (b) SLM heat-treated material, with grain boundaries extending diagonally from bottom left to upper right, aligned dislocations extending across grain boundaries indicated by the dashed lines, and precipitates (arrows). Diffraction pattern inset in (b) with spreading of diffraction peaks indicative of  $5.7^\circ$  misorientations between grains.

Si- enrichment. Frequently, precipitates were surrounded by tangled, pinned dislocations in the heat-treated SLM structure.

### 3.3.6. Dislocation microstructures in DED

As-built DED microstructures were qualitatively less refined than as-built SLM structures, as shown in Fig. 12. The as-built DED microstructure consisted of large, dendritic dislocation cells 1–2.5  $\mu\text{m}$  in diameter, delineated by the large dashed line in Fig. 12(a), superimposed on a background of smaller, equiaxed dislocation cells with an average diameter approximately 370 nm in diameter. The large cell structures consisted of dislocations with Cr segregation and Fe depletion in the walls, indicating that they are dendritic, while the small cell structures exhibited uniform composition. Although the large, dendritic dislocation walls appeared equiaxed in electron-transparent foils, FIB machining and SEM analysis indicated that these walls were elongated similar to the SLM dislocation cells, but in the foil normal direction (which coincides with the build direction). The small dislocation cells with uniform composition were not found to be elongated. Both types of

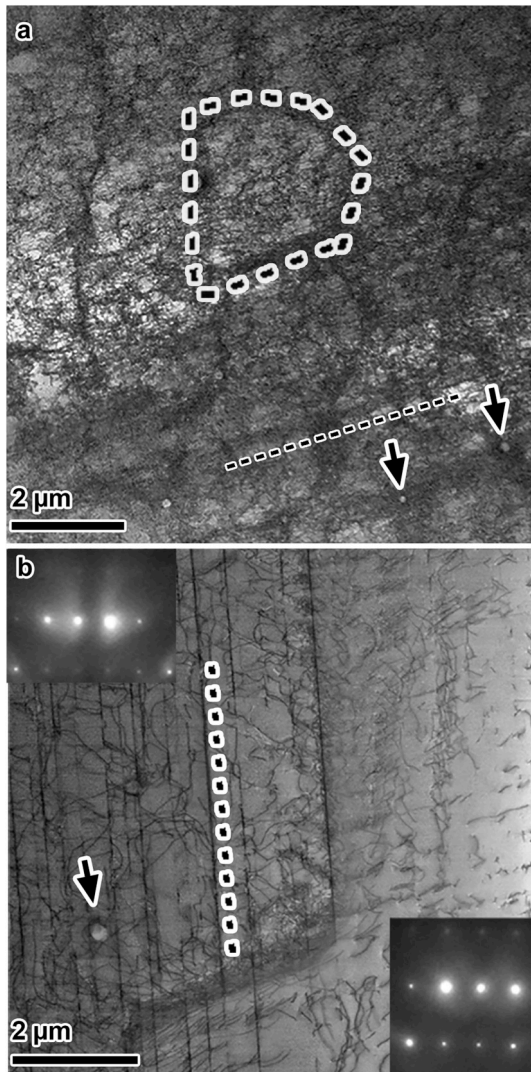


**Fig. 12.** Bright-field diffraction-contrast STEM images of dislocation structures in (a) DED as-built material, with extended dislocation walls (parallel to the small dashed line), precipitates (arrows), and dendritic dislocation walls (outlined by the large dashed line) surrounding small, equiaxed dislocation cells. (b) DED heat-treated material with precipitates (arrow), a grain boundary running from top to bottom, and dislocation pileups on  $\{111\}$  planes (parallel to the dashed line) near grain boundaries. Inset diffraction patterns in (b) shown for the two grains across the grain boundary.

DED dislocation structures appeared qualitatively less dense than the cell walls in the SLM as-built structure, for example compare the wall indicated by the dashed line in Fig. 12(a) with that in Fig. 11(a). Additionally, a significant density of dislocation walls and tangles aligned on multiple  $\{111\}$ -type planes were observed, for example parallel to the small, straight dashed line in Fig. 11(a). These structures were typically spaced 1–2  $\mu\text{m}$  apart and extended across multiple large and small cells. Precipitates were observed throughout the microstructure, although more frequently in the walls of the large cells with segregation, and ranged in size from 70–200 nm; examples are arrowed in Fig. 12(a). Precipitates in as-built DED material were Si- and Mn-rich oxides.

Heat treatment of the DED material induced a decrease in dislocation density, as shown in the image taken across a grain boundary in Fig. 12 (b). Dislocations accumulated in the proximity of grain boundaries, such that structures were sparser in grain interiors than those shown in Fig. 12(b). Dislocation pileups were found on  $\{111\}$ -type planes near grain boundaries, as indicated by the dashed lines in Fig. 12(b). These

pileups consisted primarily of aligned dislocations with few dislocation tangles, although dislocations became more tangled with 1–2  $\mu\text{m}$  of grain boundaries. Occasionally, extended dislocations, dislocation dipoles, or nodes were observed. Precipitates were less frequently observed, and those that remained ranged from 150–250 nm in size, for example as indicated by the arrow in Fig. 12(b). These precipitates were found both in the matrix and along grain boundaries and were primarily Mn- and Cr-rich oxides without Si enrichment.

#### 4. Discussion

The influence of AM processing on microstructures has important implications for mechanical properties, and consequently TO design. These implications are summarized in Fig. 13 in the form of an influence diagram that can help guide the decision-making process in DfAM. The diagram depicts the TO for the AM process as a closed loop, where changes in one step can affect the entire process. The results from this study indicate that until a holistic optimization framework is developed which encompasses all the steps included in Fig. 13, TO for AM must be examined and experimentally validated on a case-by-case basis due to the variance in microstructure and overall mechanical response. The difficulties in estimating the mechanical response of TO parts from FEM and material response based on AM microstructures, and the subsequent need for experimental validation, are discussed in the following sections.

##### 4.1. Prediction of yield strength based on analysis of AM microstructures

The yield strength in a material is an essential input to TO and FEM, but it can be greatly influenced by several microstructural features developed during AM, particularly the dislocation structures, grain

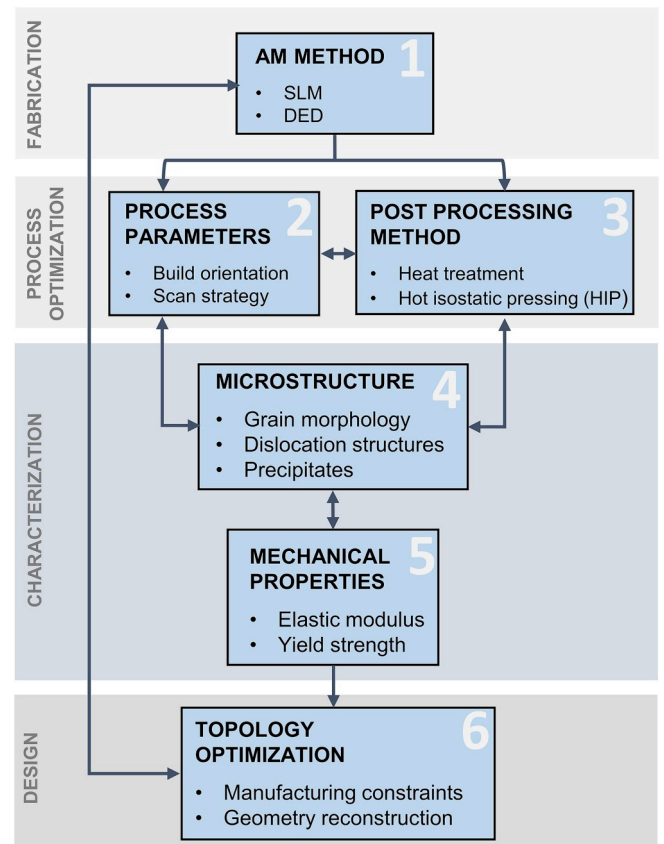


**Fig. 13.** DfAM decision-making diagram. Arrows indicate the influence of each step on the other. More items can be added to each step as our understanding of the process matures.



**Table 9**  
Summary of averaged microstructural features that may influence the yield strength.

		Equiaxed dislocation cell size (nm)	Dendritic dislocation wall spacing (nm)	Dislocation density ( $m^{-2}$ )	Precipitate diameter (nm)	Grain size ( $\mu m$ )
SLM	as-built	-	450	$3.8 \times 10^{14}$ [61]	15	20
	heat-treated	-	-	$9 \times 10^{13}$ [35]	40	16
DED	as-built	370	1750	$2.5 \times 10^{14}$ [35,60,61]	120	80
	heat-treated	-	-	$9 \times 10^{13}$ [35]	200	140

structure, and precipitate distribution. A summary of the microstructural features in the different materials is shown in Table 9. Dislocation densities are reported from the literature as measured by x-ray diffraction techniques for similar materials and heat treatments [35,60,61]. In the SLM heat-treated case, the dislocation density is estimated to be similar to that measured by Bronkhorst et al. for heat-treated DED 316L [35]. Experimental line intercept methods in this study were consistent with these published values.

The potential influences of these different parameters on the yield strength are as follows. First, increasing dislocation content increases material yield strength, and the dislocation content in the AM materials was shown to be high. The dense, elongated dislocation cells that occur in as-built SLM material, as shown in Fig. 11, are well-documented [33, 62–64], and the high yield strengths observed in SLM SS316L compared to conventional annealed material are frequently attributed to the presence of these structures. DED dislocation structures have received less attention in the literature but appear to be influential on mechanical response given the differences in mechanical response after heat treatment. Although the dislocation density remains high, structures are less organized than in SLM material, with less organization of dislocations into cell walls. Additionally, in the DED material, although segregation was observed, it did not overlap with all dislocation cells, leading to a dual cell structure with two types of walls, one dendritic with segregation and one equiaxed with uniform composition. Although outside the scope of this study, the additional solid-solution strengthening effect afforded by segregation to some of these walls would be expected to contribute to strengthening as well.

Precipitates can also strengthen the material due to particle hardening effects by presenting barriers to dislocation motion [65]. Grain morphology can also impact the mechanical response, such that decreasing grain size increases the yield strength according to the well-known Hall-Petch effect [65,66].

In order to assess the relative contributions of different microstructural features on the yield strength, calculations of the strengthening afforded by each of these microstructural features were performed. The effect of dislocation strengthening based on dislocation densities reported for similar materials in the literature [35,60,61] was estimated using a forest-hardening model, the effect of grain size was calculated via the Hall-Petch effect, and precipitate strengthening due to Orowan hardening was calculated, as summarized in Table 10. For SLM as-built material, the Hall-Petch effect was calculated treating dislocation cells as the grain size, since the walls have been shown to be effective barriers to dislocation motion and such treatment has yielded good approximations for others in the literature [33]. For other materials, the combined

**Table 10**  
Calculated contributions to yield strength based on the Hall-Petch relationship and forest dislocation strengthening, and the difference between calculated estimates and measured values. All values are in (MPa).

		Hall-Petch contribution (cell size)	Hall-Petch contribution (grain size)	Dislocation density contribution	Particle hardening	Yield based on calculated contributions	Actual yield	$\Delta$
SLM	as-built	429	-	-	65	677	560	117
	heat-treated	-	63	180 [35]	36	462	377	85
DED	as-built	-	28	300 [35,60,61]	-	511	489	22
	heat-treated	-	21	180 [35]	-	384	325	60

effects of grain size and forest dislocation hardening were used. Particle hardening was estimated for SLM material, using estimates of the volume fraction of precipitates as reported in Ref. [59].

In all cases, this approach led to overestimation of the actual hardening. The differences between actual results and microstructurally-based estimates indicate a need to validate the mechanical properties of the AM material separately before use in TO models. Not only do the microstructures vary substantially between conventional materials and AM materials, but also the same heat treatment can have different effects, as observed with grain refinement in SLM material and grain growth in DED material subject to the same heat treatment.

Dislocation density appeared to have the most significant effect on the strengthening, whether due to treating the cells as contributing to a Hall-Petch type effect or due to forest hardening. Particle hardening was not observed to be significant in the SLM material, due to the relatively low overall volume fraction of precipitates.

Grain boundary strengthening similarly appeared to contribute little to the total strengthening. For SLM as-built material, the thin, columnar grains and dislocation cells contribute to an enhanced yield strength compared to many conventional recrystallized materials with grain sizes on the order of 50–100  $\mu m$  [33], or for example the DED materials. Upon heat treatment, the particular rearrangement of the dislocation structures only slightly influenced the grain structure in the SLM materials, although the heat-treated structures were significantly different than the preexisting dislocation cells. This suggests that the grain structure was not as influential a factor in determining the overall yield strength as the dislocation structures.

In DED as-built material, the grain size alone fell within the range of about 20–120  $\mu m$  in diameter and is not expected to have significantly influenced yield compared to conventional material. The heat treatment of DED material caused grain growth, but the yield strength after heat treatment was approximately 67% of the initial yield strength. This is an equivalent yield drop to that observed in SLM specimens with heat treatment, even though the grain sizes barely changed in the SLM specimens, indicating that grain size had less influence on yield in the AM materials than other factors like dislocation structure. Further, this indicates that the dislocation structures that developed near grain boundaries in the heat-treated DED material were more influential on the mechanical response than the grain boundaries themselves.

#### 4.2. Additional influence of TO design on strengthening

The orientation of grain boundaries may influence elastic response in different orientations. Since grains in the DED as-built material are



elongated in the laser scanning direction, the distance between grain boundaries is smaller perpendicular to the scan path than parallel to it, leading to a different effective grain size in different directions. If the material is loaded perpendicular to the laser scan path, the shorter effective grain size could lead to a greater Hall-Petch strengthening effect. This behavior was confirmed recently by Mukherjee [67], who showed that the yield strength in DED material loaded in different orientations increased with decreasing effective grain size based on the orientation of the scanning direction with respect to the loading direction. This result has important implications for TO. Since the laser scan path can affect the effective grain size in different regions, as was observed in Fig. 10, the yield strength may change locally within the part depending on the local stress state. Since TO parts typically exhibit complex, spatially-varying stress states due to their complex geometries, the interactions between processing parameters, microstructure, and properties is even more complex and difficult to predict, necessitating experimental testing prior to TO, as indicated in Fig. 13. This effect may also contribute to differences between FEM predictions and actual part performance.

#### 4.3. Influence of AM on accuracy of FEM predictions

According to Table 8, clevis samples performed better than FEM predictions in all cases. This positive deviance can be explained by considering the effects of process parameters on microstructure and the fact that FEM does not account for material anisotropy due to local microstructural variations. As indicated in Fig. 10, grain orientation and size are different on sample's periphery due to different scan strategies used to print the outline (shell) of the clevis, particularly in DED samples. It so happens that the maximum von Mises stress occurs on the sample's periphery where this microstructure refinement takes place. As a result, samples exhibited higher yield loads than FEM predictions. This result was more pronounced for DED samples according to Fig. 10. Moreover, the DED clevises had 11.8% more volume than the model used in FEM, which if not accounted for, can result in larger deviations from FEM predictions. For more accurate results, machine manufacturers can implement scaling factors in their part-preparation software to correct for this manufacturing induced enlargement.

#### 4.4. Potential benefits of AM for TO

Understanding the PSPP relationship within the context of TO has the potential to become a powerful tool. Exploiting this relationship may allow manufacturers to: create parts that are better suited for tension or compression in different areas of the part (by manipulating texture or grain boundary orientation); change the mechanical response by changing laser scan strategy to have different grain orientations, elongations, or sizes; and to adjust the microstructure to have maximum strength in some areas and maximum ductility in others, all dependent on what is most beneficial within the complex stress fields that correspond to these complex geometries. In other words, there is opportunity to exceed the current practices of design optimization; to simultaneously optimize process parameters, microstructure features, and final topology to achieve properties that are locally tailored to specific applications at the voxel level [13,68].

## 5. Conclusions

In this paper, topology optimized designs were manufactured using SLM and DED methods and their mechanical performance were experimentally compared with FEM. Effects of AM method and heat treatment on microstructure were studied and correlated to mechanical properties that are essential in TO. Discrepancies between the FEM and experimental results were investigated and correlated to process-induced microstructure features in clevis samples. The following conclusions can be drawn from the experimental results:

- Topology optimized clevis samples outperformed the FEM predictions for both SLM and DED methods by 6% and 29% in as-built state, and 18% and 38% in heat-treated state, respectively. This difference is attributed to changes in the microstructure of the boundary (shell) layers that is caused by different scan strategies and process parameters used to fabricate those layers. In SLM, grain size and alignment between scan path direction were changed whereas in DED, grain size and grain elongation direction were changed. These microstructure alterations strengthened regions of the sample where the maximum von Mises stress occurred, resulting in higher yield loads. Typical FEM does not consider such manufacturing-induced anisotropies, suggesting that more mesoscale-based models would help refine the conservative estimates.
- SLM samples showed higher yield strength compared to DED, and they both showed higher yield strength compared to conventionally-made SS316L. The most influential microstructural feature in increasing the yield strength proved to be the dislocation structures in both AM methods, in as-built and heat-treated states, whereas grain size contribution was not as significant. The difference in yield strength between SLM and DED was partially responsible for the slight difference in the optimal topologies computed for both AM methods.

In summary, the topology optimization approach was shown to be sensitive to AM method, process parameters and heat treatment. The main differences are attributed to the varied microstructural evolutions, illustrating a need for a comprehensive understanding of the PSPP relationships to provide holistic design optimization schemes.

#### Declaration of competing interest

The authors declare the following financial interests/personal relationships which may be considered as potential competing interests: Prof. Suresh is a consulting Chief Scientific Officer of SciArt, Corp, which has licensed the Pareto technology, developed in Prof. Suresh's lab, through Wisconsin Alumni Research Foundation.

#### CRediT authorship contribution statement

**B. Rankouhi:** Conceptualization, Methodology, Data curation, Writing - original draft. **K.M. Bertsch:** Conceptualization, Methodology, Data curation, Writing - original draft. **G. Meric de Bellefon:** Data curation, Writing - review & editing. **M. Thevamaran:** Data curation. **D. J. Thoma:** Supervision, Writing - review & editing. **K. Suresh:** Supervision, Writing - review & editing.

#### Acknowledgments

The authors would like to acknowledge the support from National Science Foundation (NSF) through the grant CMMI-1561899 and NSF-DMREF through the grant DMR-1728933. Authors would also like to thank the Grainger Institute for Engineering for seeding the research activity. The EOS M290 was supported with UW2020 WARF Discovery Institute funds.

#### References

- [1] I. Wohlers Associates, report Wohlers Report 2017 : 3D Printing and Additive Manufacturing State of the Industry : Annual Worldwide Progress Report., n.d. <https://wohlersassociates.com/2017report.htm> (accessed November 4, 2018).
- [2] C.L. Benson, G. Triulzi, C.L. Magee, Is there a Moore's law for 3D printing? 3D Print. Addit. Manuf. 5 (2018) 53–62, <https://doi.org/10.1089/3dp.2017.0041>.
- [3] T.T. Wohlers, (Specialist in three dimensional printing), I. Campbell, O. Diegel, J. Kowen, Wohlers report 2018 : report 3D Printing and Additive Manufacturing State of the Industry : Annual Worldwide Progress Report., n.d.
- [4] J. Liu, A.T. Gaynor, S. Chen, Z. Kang, K. Suresh, A. Takezawa, L. Li, J. Kato, J. Tang, C.C.L. Wang, L. Cheng, X. Liang, A.C. To, Current and future trends in topology

- optimization for additive manufacturing, *Struct. Multidiscip. Optim.* 57 (2018) 2457–2483, <https://doi.org/10.1007/s00158-018-1994-3>.
- [5] A.T. Gaynor, J.K. Guest, Topology optimization considering overhang constraints: eliminating sacrificial support material in additive manufacturing through design, *Struct. Multidiscip. Optim.* 54 (2016) 1157–1172, <https://doi.org/10.1007/s00158-016-1551-x>.
- [6] A.M. Mirzendehehd, K. Suresh, Support structure constrained topology optimization for additive manufacturing, *Comput. Des.* 81 (2016) 1–13, <https://doi.org/10.1016/J.CAD.2016.08.006>.
- [7] X. Wang, S. Xu, S. Zhou, W. Xu, M. Leary, P. Choong, M. Qian, M. Brandt, Y.M. Xie, Topological design and additive manufacturing of porous metals for bone scaffolds and orthopaedic implants: a review, *Biomaterials* 83 (2016) 127–141, <https://doi.org/10.1016/J.BIOMATERIALS.2016.01.012>.
- [8] A.M. Mirzendehehd, B. Rankouhi, K. Suresh, Strength-based topology optimization for anisotropic parts, *Addit. Manuf.* 19 (2018) 104–113, <https://doi.org/10.1016/j.addma.2017.11.007>.
- [9] P. Zhang, J. Liu, A.C. To, Role of anisotropic properties on topology optimization of additive manufactured load bearing structures, *Scripta Mater.* 135 (2017) 148–152, <https://doi.org/10.1016/J.SCRIPTAMAT.2016.10.021>.
- [10] M. Seabra, J. Azevedo, A. Araújo, L. Reis, E. Pinto, N. Alves, R. Santos, J. Pedro Mortágua, Selective laser melting (SLM) and topology optimization for lighter aerospace components, *Procedia Struct. Integr.* 1 (2016) 289–296, <https://doi.org/10.1016/J.PROSTR.2016.02.039>.
- [11] S. Yoder, S. Morgan, C. Kinzy, E. Barnes, M. Kirka, V. Paquit, P. Nandwana, A. Plotkowski, R.R. Dehoff, S.S. Babu, Characterization of topology optimized Ti-6Al-4V components using electron beam powder bed fusion, *Addit. Manuf.* 19 (2017) 184–196, <https://doi.org/10.1016/j.addma.2017.12.001>.
- [12] M.E. Lynch, M. Mordasky, L. Cheng, A. To, Design, testing, and mechanical behavior of additively manufactured casing with optimized lattice structure, *Addit. Manuf.* 22 (2018) 462–471, <https://doi.org/10.1016/J.ADDMA.2018.05.021>.
- [13] B.H. Jared, M.A. Aguiló, L.L. Beghini, B.L. Boyce, B.W. Clark, A. Cook, B.J. Kaehr, J. Robbins, Additive manufacturing: toward holistic design, *Scripta Mater.* 135 (2017) 141–147, <https://doi.org/10.1016/J.SCRIPTAMAT.2017.02.029>.
- [14] I. Gibson, D. Rosen, B. Stuecker, Additive Manufacturing Technologies, Springer New York, New York, NY, 2015, <https://doi.org/10.1007/978-1-4939-2113-3>.
- [15] B.E. Carroll, R.A. Otis, J.P. Borgonia, J. Suh, R.P. Dillon, A.A. Shapiro, D. Hofmann, Z.-K. Liu, A.M. Beese, Functionally graded material of 304L stainless steel and inconel 625 fabricated by directed energy deposition: characterization and thermodynamic modeling, *Acta Mater.* 108 (2016) 46–54, <https://doi.org/10.1016/J.ACTAMAT.2016.02.019>.
- [16] R.M. Mahmood, E.T. Akinlabi, Laser metal deposition of functionally graded Ti6Al4V/TiC, *Mater. Des.* 84 (2015) 402–410, <https://doi.org/10.1016/J.MATDES.2015.06.135>.
- [17] K. Shah, I. ul Haq, A. Khan, S.A. Shah, M. Khan, A.J. Pinkerton, Parametric study of development of Inconel-steel functionally graded materials by laser direct metal deposition, *Mater. Des.* 54 (2014) 531–538, <https://doi.org/10.1016/J.MATDES.2013.08.079>.
- [18] W. Li, S. Karnati, C. Kriewall, F. Liou, J. Newkirk, K.M.B. Taming, W.J. Seufzer, K.M. Brown Taming, W.J. Seufzer, Fabrication and characterization of a functionally graded material from Ti-6Al-4 V to SS316 by laser metal deposition, *Addit. Manuf.* 14 (2017) 95–104, <https://doi.org/10.1016/j.addma.2016.12.006>.
- [19] A.M. Mirzendehehd, K. Suresh, A pareto-optimal approach to multimaterial topology optimization, *J. Mech. Des.* 137 (2015) 101701, <https://doi.org/10.1115/1.4031088>.
- [20] J.A. Cherry, H.M. Davies, S. Mehmood, N.P. Lavery, S.G.R. Brown, J. Sieng, Investigation into the effect of process parameters on microstructural and physical properties of 316L stainless steel parts by selective laser melting, *Int. J. Adv. Manuf. Technol.* 76 (2015) 869–879, <https://doi.org/10.1007/s00170-014-6297-2>.
- [21] A. Ahmadi, R. Mirzaeifar, N.S. Moghaddam, A.S. Turabi, H.E. Karaca, M. Elahinia, Effect of manufacturing parameters on mechanical properties of 316L stainless steel parts fabricated by selective laser melting: a computational framework, *Mater. Des.* 112 (2016) 328–338, <https://doi.org/10.1016/J.MATDES.2016.09.043>.
- [22] T. Kurzynowski, K. Gruber, W. Stopyra, B. Kuźnicka, E. Chleb, Correlation between process parameters, microstructure and properties of 316 L stainless steel processed by selective laser melting, *Mater. Sci. Eng.* 718 (2018) 64–73, <https://doi.org/10.1016/J.MSEA.2018.01.103>.
- [23] E. Liverani, S. Toschi, L. Ceschini, A. Fortunato, Effect of selective laser melting (SLM) process parameters on microstructure and mechanical properties of 316L austenitic stainless steel, *J. Mater. Process. Technol.* 249 (2017) 255–263, <https://doi.org/10.1016/J.JMATPROTEC.2017.05.042>.
- [24] Z. Sun, X. Tan, S. Tor, C.C.-N.A. Materials, undefined 2018, Simultaneously Enhanced Strength and Ductility for 3D-Printed Stainless Steel 316L by Selective Laser Melting, *Nature.Com.* (n.d.). <https://www.nature.com/articles/s41427-018-0018-5> (accessed November 9, 2018).
- [25] J.J. Lewandowski, M. Seifi, Metal additive manufacturing: a review of mechanical properties, *Annu. Rev. Mater. Res.* 46 (2016) 151–186, <https://doi.org/10.1146/annurev-matsci-070115-032024>.
- [26] M.F. Zaeh, G. Branner, Investigations on residual stresses and deformations in selective laser melting, *Prod. Eng.* 4 (2010) 35–45, <https://doi.org/10.1007/s11740-009-0192-y>.
- [27] P. Mercelis, J. Kruth, Residual stresses in selective laser sintering and selective laser melting, *Rapid Prototyp. J.* 12 (2006) 254–265, <https://doi.org/10.1108/13552540610707013>.
- [28] P. Guo, B. Zou, C. Huang, H. Gao, Journal of Materials Processing Technology Study on Microstructure, Mechanical Properties and Machinability of Efficiently Additive Manufactured AISI 316L Stainless Steel by High-Power Direct Laser Deposition, vol. 240, Elsevier, 2017, pp. 12–22, <https://doi.org/10.1016/J.JMATPROTEC.2016.09.005>.
- [29] K. Zhang, S. Wang, W. Liu, X. Shang, Characterization of stainless steel parts by laser metal deposition shaping, *Mater. Des.* 55 (2014) 104–119, <https://doi.org/10.1016/j.matdes.2013.09.006>.
- [30] K. Ohnishi, T. Ohnishi, The biological effects of space radiation during long stays in space, *Biol. Sci. Space* 18 (2004) 201–205, <https://doi.org/10.2187/bss.18.201>.
- [31] N. Shamsaei, A. Yadollahi, L. Bian, S.M. Thompson, An overview of Direct Laser Deposition for additive manufacturing; Part II: mechanical behavior, process parameter optimization and control, *Addit. Manuf.* 8 (2015) 12–35, <https://doi.org/10.1016/J.ADDMA.2015.07.002>.
- [32] T. DebRoy, H.L. Wei, J.S. Zuback, T. Mukherjee, J.W. Elmer, J.O. Milewski, A. M. Beese, A. Wilson-Heid, A. De, W. Zhang, Additive manufacturing of metallic components – process, structure and properties, *Prog. Mater. Sci.* 92 (2018) 112–224, <https://doi.org/10.1016/J.PMATSCI.2017.10.001>.
- [33] Y.M. Wang, T. Voisin, J.T. McKeown, J. Ye, N.P. Cailta, Z. Li, Z. Zeng, Y. Zhang, W. Chen, T.T. Roehling, R.T. Ott, M.K. Santala, P.J. Depond, M.J. Matthews, A. V. Hamza, T. Zhu, Additively manufactured hierarchical stainless steels with high strength and ductility, *Nat. Mater.* 17 (2018), <http://www.nature.com/articles/nmat5021>, accessed May 31, 2019.
- [34] M. Mukherjee, Effect of build geometry and orientation on microstructure and properties of additively manufactured 316L stainless steel by laser metal deposition, *Materialia* 7 (2019) 100359, <https://doi.org/10.1016/J.MTLA.2019.100359>.
- [35] C.A. Bronkhorst, J.R. Mayeur, V. Livescu, R. Pokharel, D.W. Brown, G.T. Gray, Structural representation of additively manufactured 316L austenitic stainless steel, *Int. J. Plast.* 118 (2019) 70–86, <https://doi.org/10.1016/J.IJPLAS.2019.01.012>.
- [36] L. Liu, Q. Ding, Y. Zhong, J. Zou, J. Wu, Y.-L. Chiu, J. Li, Z. Zhang, Q. Yu, Z. Shen, Dislocation network in additive manufactured steel breaks strength–ductility trade-off, *Mater. Today* 21 (2018) 354–361, <https://doi.org/10.1016/J.MATTOD.2017.11.004>.
- [37] T.R. Smith, J.D. Sugar, C. San Marchi, J.M. Schoenung, Strengthening mechanisms in directed energy deposited austenitic stainless steel, *Acta Mater.* 164 (2019) 728–740, <https://doi.org/10.1016/J.ACTAMAT.2018.11.021>.
- [38] M. Shamsujjoha, S.R. Agnew, J.M. Fitz-Gerald, W.R. Moore, T.A. Newman, High strength and ductility of additively manufactured 316L stainless steel explained, *Metall. Mater. Trans.* 49 (2018) 3011–3027, <https://doi.org/10.1007/s11661-018-4607-2>.
- [39] M. Ma, Z. Wang, X. Zeng, A comparison on metallurgical behaviors of 316L stainless steel by selective laser melting and laser cladding deposition, *Mater. Sci. Eng.* 685 (2017) 265–273, <https://doi.org/10.1016/J.MSEA.2016.12.112>.
- [40] M. Ziętala, T. Durejko, M. Polański, I. Kunce, T. Płocinski, W. Zieliński, M. Łazińska, W. Stepiński, T. Czujko, K.J. Kurzydowski, Z. Bojar, The microstructure, mechanical properties and corrosion resistance of 316 L stainless steel fabricated using laser engineered net shaping, *Mater. Sci. Eng.* 677 (2016) 1–10, <https://doi.org/10.1016/J.MSEA.2016.09.028>.
- [41] A. Yadollahi, N. Shamsaei, S.M. Thompson, D.W. Seely, Effects of process time interval and heat treatment on the mechanical and microstructural properties of direct laser deposited 316L stainless steel, *Mater. Sci. Eng.* 644 (2015) 171–183, <https://doi.org/10.1016/J.MSEA.2015.07.056>.
- [42] ASTM A276, Standard Specification for Stainless Steel Bars and Shapes, 2016, <https://doi.org/10.1520/A0276>.
- [43] K. Suresh, Efficient generation of large-scale pareto-optimal topologies, *Struct. Multidiscip. Optim.* 47 (2013) 49–61, <https://doi.org/10.1007/s00158-012-0807-3>.
- [44] A. Mirzendehehd, S. Krishnan, [manufacturer not identified], A hands-on introduction to topology optimization, n.d. <https://olin.tind.io/record/1588291> (accessed August 26, 2019).
- [45] EOS GmbH - Electro Optical Systems, Material Data Sheet - EOS StainlessSteel 316L, 2014. [www.eos.info](http://www.eos.info), accessed November 8, 2018.
- [46] J.D. Fritz, Heat Treating of Austenitic and Duplex Stainless Steels, Heat Treat. Irons Steels. 4D, 2014, <https://doi.org/10.31399/asm.hb.v04d.a0005990>, 0.
- [47] Y. Liu, Y. Yang, D. Wang, A study on the residual stress during selective laser melting (SLM) of metallic powder, *Int. J. Adv. Manuf. Technol.* 87 (2016) 647–656, <https://doi.org/10.1007/s00170-016-8466-y>.
- [48] A. Koguchi, N. Kikuchi, A surface reconstruction algorithm for topology optimization, *Eng. Comput.* 22 (2006) 1–10, <https://doi.org/10.1007/s00366-006-0023-0>.
- [49] S. Liu, Q. Li, J. Liu, W. Chen, Y. Zhang, A realization method for transforming a topology optimization design into additive manufacturing structures, *Engineering* 4 (2018) 277–285, <https://doi.org/10.1016/J.ENG.2017.09.002>.
- [50] A. Nana, J.-C. Cuillière, V. Francois, Automatic reconstruction of beam structures from 3D topology optimization results, *Comput. Struct.* 189 (2017) 62–82, <https://doi.org/10.1016/J.COMPSTRUC.2017.04.018>.
- [51] D. Brackett, I. Ashcroft, R. Hague, Topology optimization for additive manufacturing, Sfsymposium. Engr. Utxas. Edu. (n.d.). <https://sfsymposium.engr.utexas.edu/Manuscripts/2011/2011-27-Brackett.pdf> (accessed June 18, 2019).
- [52] K. Saedi, L. Kevetkova, F. Lofaj, Z. Shen, Novel ferritic stainless steel formed by laser melting from duplex stainless steel powder with advanced mechanical properties and high ductility, *Mater. Sci. Eng.* 665 (2016) 59–65, <https://doi.org/10.1016/J.MSEA.2016.04.027>.

- [53] T.R. Smith, J.D. Sugar, J.M. Schoenung, C. San Marchi, Anomalous annealing response of directed energy deposited type 304L austenitic stainless steel, *JOM (J. Occup. Med.)* 70 (2018) 358–363, <https://doi.org/10.1007/s11837-017-2711-1>.
- [54] D. Zhang, W. Niu, X. Cao, Z. Liu, Effect of standard heat treatment on the microstructure and mechanical properties of selective laser melting manufactured Inconel 718 superalloy, *Mater. Sci. Eng.* 644 (2015) 32–40, <https://doi.org/10.1016/J.MSEA.2015.06.021>.
- [55] M.P. Chae, W.M. Rozen, P.G. McMenamin, M.W. Findlay, R.T. Spychal, D. J. Hunter-Smith, Emerging applications of bedside 3D printing in plastic surgery, *Front. Surg.* 2 (2015) 25, <https://doi.org/10.3389/fsurg.2015.00025>.
- [56] K. Saeidi, F. Akhtar, Subgrain-controlled grain growth in the laser-melted 316 L promoting strength at high temperatures, *R. Soc. Open Sci.* 5 (2018) 172394, <https://doi.org/10.1098/rsos.172394>.
- [57] D. Kong, C. Dong, X. Ni, L. Zhang, J. Yao, C. Man, X. Cheng, K. Xiao, X. Li, Mechanical properties and corrosion behavior of selective laser melted 316L stainless steel after different heat treatment processes, *J. Mater. Sci. Technol.* 35 (2019) 1499–1507, <https://doi.org/10.1016/J.JMST.2019.03.003>.
- [59] G. Meric de Bellefon, K.M. Bertsch, M.R. Chancey, Y.Q. Wang, D.J. Thoma, Influence of solidification structures on radiation-induced swelling in an additively-manufactured austenitic stainless steel, *J. Nucl. Mater.* 523 (2019) 291–298, <https://doi.org/10.1016/J.JNUCMAT.2019.06.012>.
- [60] D.W. Brown, D.P. Adams, L. Balogh, J.S. Carpenter, B. Clausen, G. King, B. Reedlunn, T.A. Palmer, M.C. Maguire, S.C. Vogel, In situ neutron diffraction study of the influence of microstructure on the mechanical response of additively manufactured 304L stainless steel, *Metall. Mater. Trans.* 48 (2017) 6055–6069, <https://doi.org/10.1007/s11661-017-4330-4>.
- [61] R. Pokharel, L. Balogh, D.W. Brown, B. Clausen, G.T. Gray, V. Livescu, S.C. Vogel, S. Takajo, Signatures of the unique microstructure of additively manufactured steel observed via diffraction, *Scripta Mater.* 155 (2018) 16–20, <https://doi.org/10.1016/J.SCRIPTAMAT.2018.06.008>.
- [62] A. Röttger, K. Geenen, M. Windmann, F. Binner, W. Theisen, Comparison of microstructure and mechanical properties of 316 L austenitic steel processed by selective laser melting with hot-isostatic pressed and cast material, *Mater. Sci. Eng.* 678 (2016) 365–376, <https://doi.org/10.1016/J.MSEA.2016.10.012>.
- [63] T. Niendorf, S. Leuders, A. Riemer, H.A. Richard, T. Tröster, D. Schwarze, Highly anisotropic steel processed by selective laser melting, *Metall. Mater. Trans. B* 44 (2013) 794–796, <https://doi.org/10.1007/s11663-013-9875-z>.
- [64] F. Yan, W. Xiong, E. Faierson, F. Yan, W. Xiong, E.J. Faierson, Grain structure control of additively manufactured metallic materials, *Materials* 10 (2017) 1260, <https://doi.org/10.3390/ma10111260>.
- [65] G. Dieter, D. Bacon, *Mechanical Metallurgy*, 1986. <http://www.academia.edu/download/30977829/3393.pdf>. accessed June 24, 2019.
- [66] N. Hansen, Hall–Petch relation and boundary strengthening, *Scripta Mater.* 51 (2004) 801–806, <https://doi.org/10.1016/J.SCRIPTAMAT.2004.06.002>.
- [67] M. Mukherjee, Effect of build geometry and orientation on microstructure and properties of additively manufactured 316L stainless steel by laser metal deposition, *Materialia* 7 (2019) 100359, <https://doi.org/10.1016/J.MTLA.2019.100359>.
- [68] J. Zowe, M. Kočvara, M.P. Bendsøe, Free material optimization via mathematical programming, *Math. Program.* 79 (1997) 445–466, <https://doi.org/10.1007/BF02614328>.